Multiplex FET biosensor with vapor-deposited molecularly imprinted nanotubes for cancer biomarkers

Nanotechnology

OPEN ACCESS

RECEIVED
5 October 2025

REVISED
27 March 2026

ACCEPTED FOR PUBLICATION
14 April 2026

PUBLISHED
30 April 2026

PAPER

Multiplex FET biosensor with vapor-deposited molecularly imprinted nanotubes for cancer biomarkers

Faruk Can[1,2], **Ufuk Ulaş Tokat**[1], **Elaheh Yousefimiab**[1], **Ali Sarp Ebil**[1], **Selma Takmaklı**[1] and **Gozde Ozaydin Ince**[1,2,3,*]

[1] Materials Science and Nanoengineering Program, Faculty of Engineering and Natural Sciences, Sabanci University, Istanbul 34956, Türkiye
[2] Nanotechnology Research and Application Center (SUNUM), Sabanci University, Istanbul 34956, Türkiye
[3] Center of Excellence for Functional Surfaces and Interfaces (EFSUN), Sabanci University, Istanbul 34956, Türkiye
[*] Author to whom any correspondence should be addressed.

E-mail: gozde.ince@sabanciuniv.edu

Keywords: CA125, HE4, FET biosensor, molecularly imprinted polymer, polypyrrole nanotube, vapor deposition polymerization

Abstract

Molecularly imprinted polymer (MIP) interfaces offer antibody-level selectivity without bioreceptor instability, yet their integration into transistor-based sensors remains limited. In this study, we present a novel multiplex field-effect transistor (FET) biosensor platform based on molecularly imprinted polypyrrole (PPy) nanotubes, synthesized through a template-assisted vapor deposition polymerization technique. The molecular imprinting process was employed to create specific recognition sites for the ovarian cancer biomarkers HE4 and CA125, enabling selective and sensitive detection of both biomarkers simultaneously. The molecularly imprinted PPy (MIP) nanotubes were fabricated with high uniformity, as confirmed by scanning electron microscopy (SEM), while Fourier-transform infrared spectroscopy (FTIR) verified the chemical composition. The dual-channel FET showed sensitivities of 0.06 $(\text{U ml}^{-1})^{-1}$ for CA125 and 0.22 pM^{-1} for HE4, limits of detection of 0.4 U ml^{-1} and 0.2 pM, and linear ranges of 0.1–25 U ml^{-1} (CA125) and 0.05–10 pM (HE4). Selectivity factors of 11.3 and 23.7 were obtained for the CA125 sensor and the HE4 sensor, respectively, indicating high specificity of the imprinted sensors for their respective target biomarkers. By combining vapor-deposited MIP nanotubes with a compact FET architecture, our work offers a promising route toward early, point-of-care diagnosis through the simultaneous quantification of multiple cancer biomarkers.

1. Introduction

Early diagnosis of cancer, which requires detection of cancer biomarkers at very low concentrations, significantly improves therapeutic outcomes [1]. Among various detection methods, antibody-based immunoassays, such as enzyme-linked immunosorbent assay, radioimmunoassay, fluoro-immunoassay, chemiluminescence-based immunoassay, and electrochemiluminescence assays, are widely employed methods due to their high sensitivity and selectivity [2, 3]. However, the majority of these methods utilize biological receptors like antibodies and enzymes, which are sensitive to environmental conditions and may affect their performance and reduce diagnostic accuracy [4]. Furthermore, strict requirements on storage conditions and limited shelf-life are current challenges faced during their usage in clinical settings [5, 6].

To address these challenges, there has been a growing interest in developing novel biosensing platforms that offer improved sensitivity, specificity, and point-of-care capabilities. In recent years, field-effect transistors (FETs) have emerged as promising platforms for biosensing applications due to their high sensitivity and rapid response times [7, 8]. By integrating molecularly imprinted polymers (MIPs) into FET sensors, their performance can be significantly enhanced [9, 10]. MIPs are synthetic polymers that are designed to mimic the binding characteristics of natural receptors by incorporating specific

recognition sites tailored to target molecules. The imprinting process generates cavities complementary to the target protein in shape, size, and chemical functionality, enabling preferential rebinding and thereby improving selectivity over non-imprinted films. These materials offer several advantages over traditional antibody-based detection systems, including increased robustness, reusability, and reduced sensitivity to environmental changes [11, 12]. These allow for highly selective detection, improving the accuracy and reliability of the sensor in capturing analytes with high affinity and specificity [13, 14].

Several studies have demonstrated the successful application of MIP-based FET biosensors for detecting cancer biomarkers. For instance, Nishitani *et al* developed a MIP-based FET sensor for oligosaccharide detection, achieving high sensitivity and selectivity [15]. Similarly, Yang *et al* constructed an extended-gate FET (EG-FET) sensor with MIP-coated gold dendrites for detecting tumor necrosis factor-alpha (TNF-α), achieving excellent reproducibility and stability [16]. Bartold *et al* also employed an EG-FET chemosensor for the selective detection of matrix metalloproteinase-1 (MMP-1), further highlighting the potential of MIP-based FET platforms in biosensing applications [17]. In another study, Mukherjee *et al* developed a FET sensor based on a MIP-functionalized graphene oxide electrode for serotonin detection in unamplified serum samples [18]. Sasaki *et al* reported an electrochemically deposited MIP-based organic FET sensor for the sensitive and selective detection of cortisol in human saliva [19].

Recently, the simultaneous detection of multiple cancer biomarkers has gained significant attention, as it improves diagnostic accuracy and reduces false positives compared to single-marker analysis. Several FET-based and electrochemical biosensors have been developed to target multiple analytes in a single platform [20–22]. However, these approaches predominantly rely on immunoassay-based detection, which requires biological recognition elements such as antibodies or enzymes to functionalize the sensor surface, leading to challenges in long-term stability, storage, and overall sensor shelf-life.

Despite these advances in FET sensors, there has been limited exploration of conducting polymer nanotubes in these platforms. Kwon *et al* demonstrated the use of vascular endothelial growth factor aptamer-functionalized PPy nanotubes in a FET biosensor for the detection of femtomolar concentrations with high sensitivity [23]. Similarly, Yoon *et al* utilized aptamer-conjugated PPy nanotubes in an electrochemical sensor, which exhibited label-free protein detection capabilities [24]. However, molecularly imprinted PPy nanotubes (MIP-NT) have not yet been integrated into FET sensor platforms, particularly for the detection of CA125 in ovarian cancer diagnosis.

In this study, we present a novel FET biosensor platform based on MIP-NT for the simultaneous monitoring of ovarian cancer tumor markers, CA125 and HE4. Molecularly imprinted PPy nanotubes were selected as the sensing material as they combine synthetic molecular recognition with conductivity, thus efficiently transducing binding-induced interfacial changes into an electrical signal. In addition, the nanotube structure provided a high surface-to-volume ratio and more accessible binding sites, which contributes to improved sensitivity and response characteristics of the FET biosensor. The MIP-NTs were synthesized using a template-assisted vapor deposition polymerization technique, which allows for the controlled fabrication of nanotubes with precisely defined dimensions and binding sites. The synthesized MIP-NTs were integrated into a FET sensor platform, which bridge the source and drain electrodes, enabling efficient charge transport and selective detection of CA125 and HE4. This work demonstrates a novel biosensor design based on molecularly imprinted FET sensors for cancer biomarker detection, offering a promising approach for the early diagnosis of ovarian cancer.

2. Materials and methods

2.1. Materials

Pyrrole (98%) and ferric chloride ($FeCl_3$, $\geqslant$98%) were purchased from Sigma-Aldrich (St. Louis, MO, USA). Human CA125 (Catalog no: 30-AC21) and human HE4 (Catalog no: 30–1338) proteins were obtained from Fitzgerald Industries International (Acton, MA, USA). 3-aminopropyltrimethoxysilane (APTMS, 97%), N-Hydroxysuccinimide (NHS, >98%), and 1-(3-dimethylaminopropyl)-3-ethyl carbodiimide hydrochloride (EDC, >98%) were purchased from Alfa Aesar (Haverhill, MA, USA). Hydrochloric acid (HCl, 37%) and phosphate-buffered saline (1x PBS: 10 mM Na_2HPO_4, 1.8 mM KH_2PO_4, 137 mM NaCl, 2.7 mM KCl, pH = 7.4) tablets were purchased from Isolab (Wertheim, Germany) and MP Biomedicals (Irvine, CA, USA). Anodic aluminum oxide (AAO) membrane filters with a pore size of 200 nm were obtained from Whatman (Cytiva, Marlborough, MA, USA). A Sylgard 184 silicone elastomer kit (polydimethylsiloxane, PDMS) was purchased from Dow Corning (Midland, MI, USA).

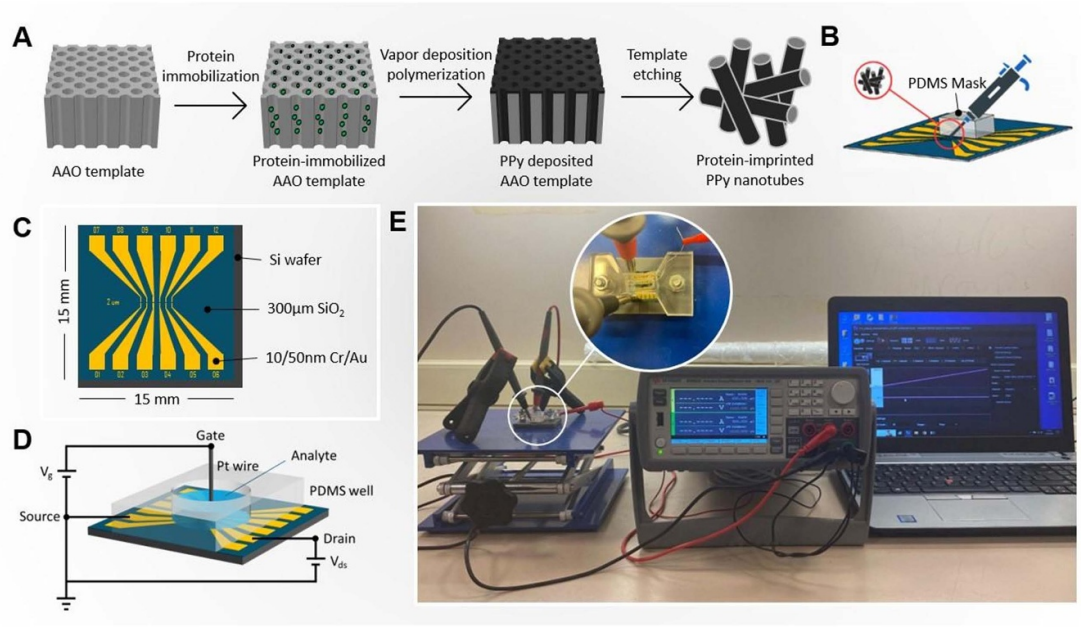

Figure 1. Schematic illustration of (A) PPy nanotube synthesis, (B) deposition of PPy on FET biosensor, (C) Microelectrode array consists of 6 pairs, and (D) solution-gated FET biosensors used in sensing applications. (E) Photo of the experimental measurement setup.

2.2. Molecularly imprinted polypyrrole nanotube synthesis

The template-assisted synthesis of molecularly imprinted PPy nanotubes (MIP-NTs) was performed using a vapor deposition polymerization technique, as described in our previous study [25]. A schematic diagram of the synthesis steps is presented in figure 1(A). Briefly, the AAO template was thoroughly cleaned in an ultrasonic bath using distilled water and ethanol to eliminate any contaminants, followed by treatment with 2.5 mL of 1% (v/v) APTMS ethanolic solution to functionalize the surface for protein binding. The membranes were then exposed to a protein solution containing 100 U ml^{-1} CA125 or 3.2 nmol ml^{-1} HE4, along with 50 mM of EDC, and 100 mM NHS in 0.1x PBS overnight at 4 °C to facilitate covalent attachment of the respective target protein.

For the fabrication of the nanotubes, CA125 and HE4 immobilized AAO template was dipped into 10% (w/v) $FeCl_3$ oxidant solution for 5 min, then dried at 40 °C. The membranes were placed in a petri dish, and 100 μL of pyrrole solution was introduced into the vacuum chamber allowing the membranes to be exposed to pyrrole vapor, initiating the polymerization. After one hour of reaction, the AAO membranes were immersed in a 2 M HCl solution for 48 h to etch the template and facilitate the release of the nanotubes. The suspensions were then centrifuged at 14 000 rpm for 10 min to collect free-standing, CA125- and HE4-imprinted PPy nanotubes, (CA125/MIP-NTs and HE4/MIP-NTs) separately. Non-imprinted PPy nanotubes (NIP-NT) were synthesized under the same conditions without the protein immobilization step for comparison.

2.3. Fabrication of FET biosensor

A microelectrode array was fabricated on a Si wafer containing a 300 μm thick SiO_2 layer through a photolithographic process. The array design consists of six pairs of rectangular Au electrodes, each 100 μm in width, with a 2 μm inter-electrode gap and a 500 μm spacing between electrode pairs (figure 1(B)). The microelectrodes were patterned with a 10 nm chromium (Cr) adhesion layer, followed by the deposition of a 50 nm gold (Au). To enable selective detection of CA125 and HE4, the six electrode pairs were divided into two functional groups. A 5 μL aliquot of CA125-imprinted PPy nanotube dispersion was drop-cast onto three electrode pairs, while an equal volume of HE4-imprinted nanotube dispersion was applied to the remaining three pairs. The sample was dried on a hotplate at 60 °C for 5 min. This deposition step was repeated two or more times to ensure consistent and stable bridge formation between the source and drain electrodes by the PPy nanotubes.

2.4. Instrumentation and measurements

Attenuated total reflectance Fourier-transform infrared spectroscopy (ATR-FTIR, Nicolet iS10, Thermo Scientific, MA, USA) was used to verify the chemical composition of the PPy, with each sample undergoing 64 consecutive scans at a resolution of 4 cm^{-1}. The formation of PPy NTs was confirmed using scanning electron microscopy (SEM, Zeiss Supra 55VP SEM-FEG, Carl Zeiss International, Oberkochen, Germany) with a 4 kV accelerating voltage. The electrical measurements were conducted using a Keysight B2902A precision source-measure unit (SMU) with Quick IV measurement software (Keysight Technologies, Santa Rosa, CA, USA). CA125 test solutions were prepared by diluting the CA125 stock solution with phosphate-buffered saline (PBS, pH 7.4) to obtain the target concentrations. The biomarker detection using the FET sensor platform was performed with an experimental setup consisting of the sensor device, PDMS well, acrylic glass chip holder, and an SMU connected to a PC for data acquisition, as shown in figure 1(D, E). The source and drain gold electrodes, and a platinum (Pt) wire acting as the gate electrode, were connected to a two-channel SMU (figure 1(C)). During the measurements, the gate voltage was fixed at 0 V while the drain voltage was swept from −0.1 V to 0.1 V at a scan rate of 2.5 mV s^{-1} at room temperature. The selectivity factor (α) for the imprinted FET sensor is calculated by taking the ratio of the sensitivities to the target and to the interferent measured on the same imprinted sensor. The sensitivity is taken as the slope of the calibration plot from separate measurements with only the target or only the interferent present, obtained under identical conditions.

3. Results and discussion

The SEM image presented in figure 2(A) shows the imprinted PPy nanotubular structures synthesized via vapor deposition polymerization, following the removal of the AAO template using 2 M HCl. The nanotubes exhibit a uniform diameter of approximately 200 nm, confirming the successful synthesis within the template. Figure 2(B) displays the FTIR spectrum of the PPy nanotubes, with characteristic absorption peaks at 1548 cm^{-1}, 1300 cm^{-1}, and 1029 cm^{-1} corresponding to C=C stretching, C–N stretching, and C–H in-plane bending vibrations within the pyrrole ring, respectively. These peaks are consistent with the expected vibrational bands of PPy, further confirming the successful polymerization achieved through the vapor deposition method. Figure 2(C) shows the SEM images of different electrodes with the nanotube channels.

Figure 3(A) illustrates the *I–V* characteristics of the CA125/MIP-NTs functionalized microelectrode, which was swept between −0.1 V and +0.1 V at a scan rate of 50 mV s^{-1} in air. The nanotubes formed a conductive bridge between the source and drain electrodes, resulting in a slope of the *I–V* curve corresponding to a conductivity (dI/dV) of 3.42×10^{-6} S. After incubation with CA125 protein, the conductivity decreased to 2.36×10^{-6} S, indicating successful binding of CA125 to the molecularly imprinted sites. Moreover, the linearity of the *I–V* curve confirms a reliable Ohmic contact between the gold electrodes and the nanotubes was achieved and maintained throughout the measurements. Figure 3(B) presents the transfer characteristics (I_{ds}–V_g) of the FET sensor prepared with CA125/MIP-NTs at a constant drain-source voltage (V_{ds}) of 100 mV. The graph shows a clear shift in drain current (I_{ds}) as the gate voltage (V_g) is varied across different concentrations of CA125. As the concentration of CA125 increases, the change in Ids becomes more prominent, particularly as Vg approaches 0 V. This behavior suggests that the redox state of the imprinted nanotubes is effectively modulated by the applied gate voltage and influenced by interaction with CA125. The favorable response of the FET sensor to increasing biomarker concentrations highlights its capability to detect CA125 efficiently, reflecting strong molecular imprinting and effective charge transport.

Figure 4 illustrates the calibration plot of the sensor response in the presence of varying concentrations of the CA125 biomarker using the FET sensor platform. The FET sensors were fabricated with CA125/MIP-NTs and NIP-NTs as control with the nanotubes forming a conductive and selective bridge between the source and drain electrodes. In figure 4(A), normalized current responses ($\Delta I/I_0$) of FET sensors prepared with CA125/MIP-NTs and NIP-NTs are compared at CA125 concentrations ranging from 0.1 to 25 U ml^{-1}. The CA125/MIP-NTs sensor demonstrates a significantly higher current response compared to the NIP FET sensor, with a linear response observed up to 25 U ml^{-1} for MIP.

This indicates that the MIP sensor has a strong binding affinity for CA125, attributed to the specific recognition sites formed within the PPy nanotubes during the molecular imprinting process. In contrast, the NIP sensor, lacking specific binding sites for CA125, exhibits a much lower and less consistent response, further confirming the selectivity of the MIP-based sensor. In figure 4(B), the sensor response is presented on a logarithmic scale to highlight the performance at lower CA125 concentrations, ranging from 0.1 to 10 U ml^{-1}. The MIP sensor shows a log-linear relationship with a regression equation of

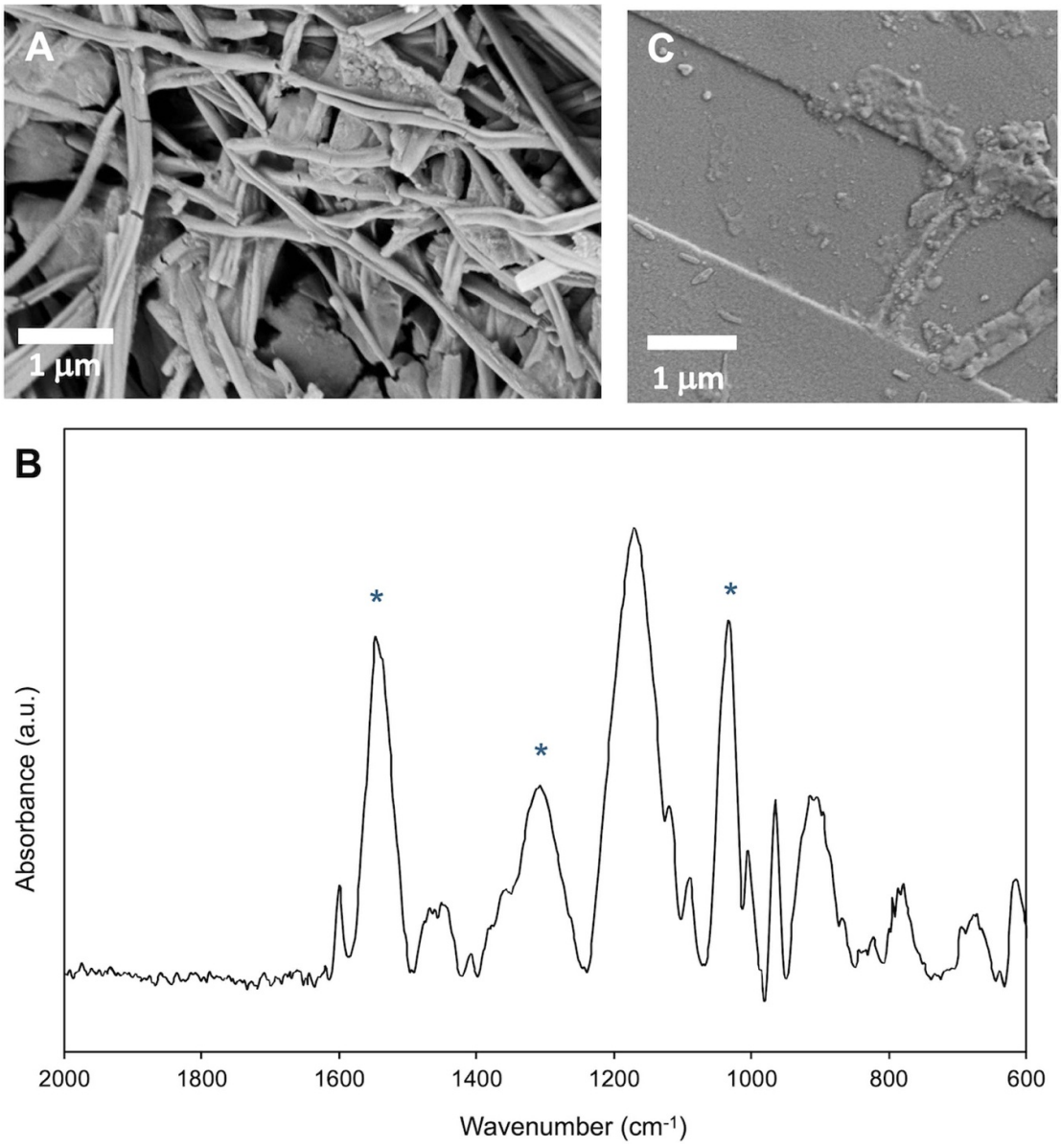

Figure 2. (A) SEM images of the MIP PPy nanotubes, (B) FTIR spectrum of the PPy nanotubes, (C) and PPy nanotubes deposited on electrodes of the FET sensor.

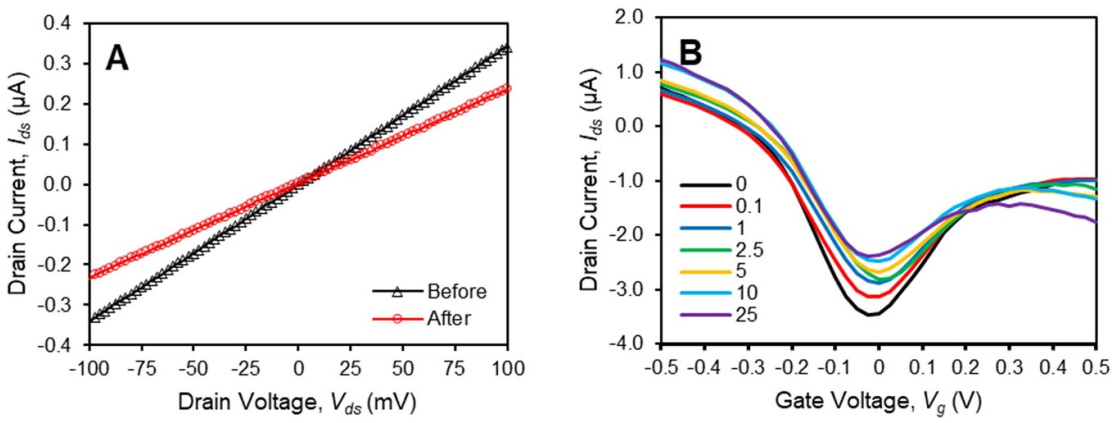

Figure 3. (A) I_{ds}–V_{ds} curves of CA125/MIP-NTs deposited on the microelectrode before and after CA125 incubation. (B) I_{ds}–V_g curves of the MI-PPy NTs FET sensor for varying CA125 concentration in U ml^{-1} (V_{ds} = 100 mV).

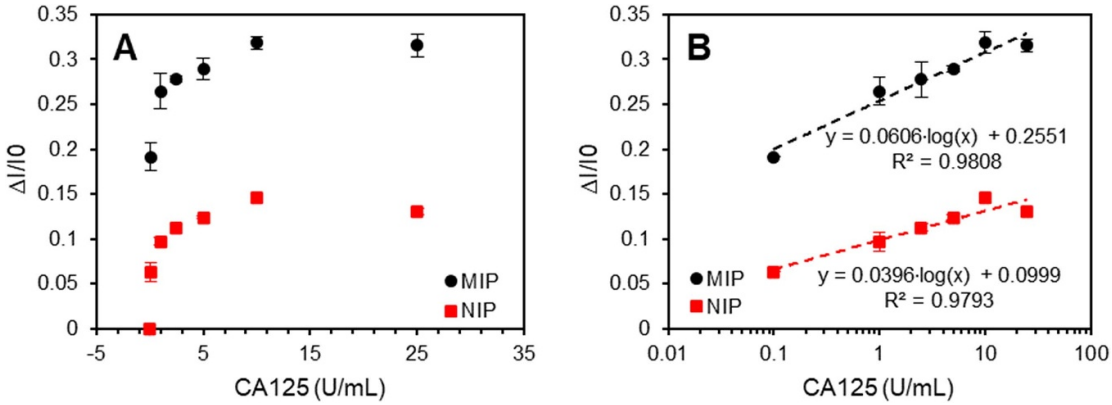

Figure 4. (A) Calibration curves of the CA125/MIP-NTs and NIP-NT biosensors for varying concentrations of the CA125 biomarker. (B) Logarithmic plot showing the sensor response across a wide range of CA125 concentrations. The MIP sensor exhibits a strong log-linear response to CA125 with a detection limit of 0.4 U ml^{-1}, whereas the NIP sensor shows a weaker response with lower sensitivity and selectivity.

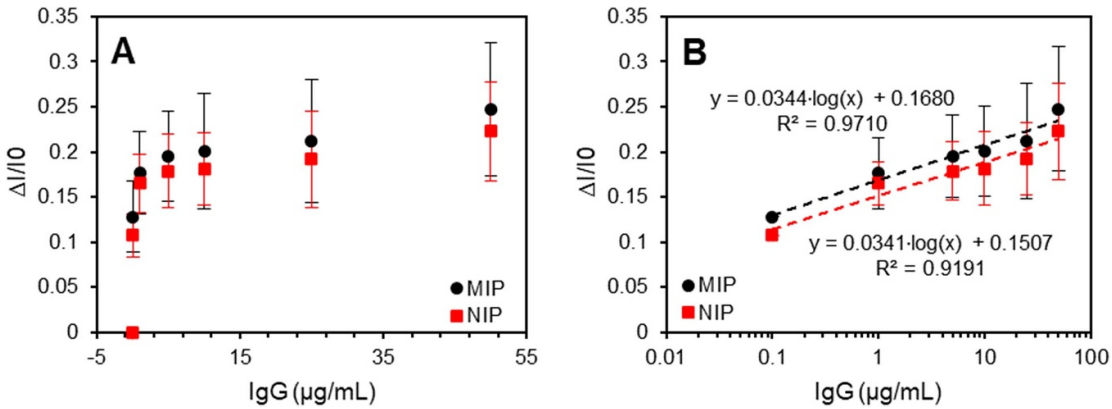

Figure 5. (A) Response of the CA125/MIP-NTs and NIP-NTs biosensors in the presence of IgG interference. (B) Logarithmic representation of sensors response to IgG. Both the MIP and NIP sensors exhibit weak and comparable log-linear responses to IgG, indicating that the response to IgG is much lower than that observed for CA125.

$y = 0.0606 \cdot \log(x) + 0.2551$ and a high correlation coefficient ($R^2 = 0.9808$), indicating a good linearity and sensitivity across a broad range of CA125 concentrations with a detection limit of 0.4 U ml^{-1} which is calculated from the equation $3\sigma/S$, where σ is the residual standard deviation of the linear regression and S is the slope of the regression line. On the other hand, the NIP sensor shows a much weaker response, with a lower slope and an R^2 value of 0.9793, indicating poor selectivity and sensitivity. These results confirm that the MIP-based FET sensor provides superior sensitivity and selectivity for CA125 detection compared to the NIP sensor. The high sensitivity, selectivity, and linearity of the MIP-based sensor can be attributed to the specific molecular imprinting of CA125 onto the PPy nanotubes, which facilitates the selective binding of the target biomarker and enables the effective detection of CA125 at clinically relevant concentrations.

Figure 5 displays the sensor response ($\Delta I/I_0$) of both CA125/MIP-NT and NIP-NT FET sensors in the presence of varying concentrations of IgG protein, which was used as an interfering molecule. In figure 5(A), the MIP sensor shows a consistent current response, although the response is notably lower compared to CA125 detection. The normalized current change reaches a plateau as the IgG concentration increases, confirming that the MIP sensor is more selective for CA125 than IgG. This is expected since the imprinted nanotubes were specifically designed for CA125. In contrast, the NIP sensor shows a more variable response, with a slightly higher interaction with IgG at some concentrations, yet still much lower than its response to CA125. This further highlights the non-specific nature of the NIP sensor. In figure 5(B), the log-scale plot provides a clearer comparison of the MIP and NIP sensor performance. The MIP sensor exhibits a weaker, yet still log-linear response to IgG with a slope of $y = 0.0344 \cdot \log(x) + 0.1680$ and an $R^2 = 0.9710$. This linearity at higher IgG concentrations suggests some interaction, but the overall response remains much lower than what was observed

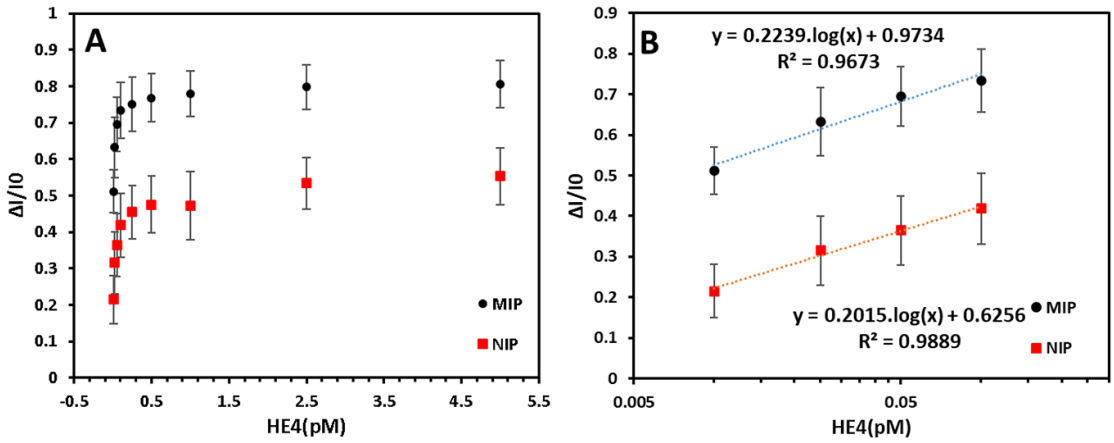

Figure 6. (A) Response of the HE4/MIP-NTs and NIP-NT FET biosensors to varying concentrations of HE4. (B) Logarithmic representation of sensor responses to HE4. The HE4/MIP-NT sensor exhibited a clear log-linear response to HE4 with a detection limit of 0.2355 pM, whereas the NIP-NT sensor showed a weaker response with lower sensitivity and selectivity.

for CA125 detection. The NIP sensor, with a regression equation of $y = 0.0341 \cdot \log(x) + 0.1507$ and $R^2 = 0.9191$, demonstrates a slightly more pronounced response to IgG, although the difference between the CA125/MIP-NT and NIP-NT sensors is less significant for IgG than for CA125.

Comparing the results between figure 4 (CA125 detection) and figure 5 (IgG detection), it is evident that the MIP sensor is highly selective for CA125, as shown by its strong and linear response in figure 4, compared to the response to IgG in figure 5, confirming the selectivity of the molecular imprinting process. The NIP sensor shows no such selectivity and demonstrates similar, weaker responses to both CA125 and IgG, further emphasizing the advantage of using molecular imprinting to enhance the selectivity and sensitivity of the FET sensor for specific biomarkers. It should also be noted that the responses observed for the NIP sensor and during the IgG interference experiments indicated the presence of non-specific protein adsorption on the PPy nanotube surface, which might be due to residual surface functionalities and the high surface area of the nanotubular structure. Still, the stronger response of the MIP sensor toward the target analytes confirmed that the imprinted cavities provided selective recognition beyond this background adsorption. In future studies, non-specific binding could be further reduced by introducing blocking or antifouling surface treatments or other passivation strategies.

Following the demonstration of selective CA125 detection, the performance of the sensors was tested for the ovarian cancer biomarker HE4, which has shown clinical relevance in early-stage disease detection and diagnosis of pelvic masses when used alongside CA125. Figure 6(A) plots the normalized current response ($\Delta I/I_0$) of the HE4/MIP-NT and NIP-NT sensors in the presence of increasing HE4 concentrations. The HE4/MIP-NT sensor shows a substantially stronger signal across all concentrations, indicating successful molecular imprinting and selective HE4 binding, while the NIP-NT sensor response remains comparatively low. Figure 6(B) shows the logarithmic representation of the sensor response, revealing a log-linear relationship, with a regression equation of $y = 0.2239 \cdot \log(x) + 0.9734$ and a high correlation coefficient ($R^2 = 0.9673$) for the HE4/MIP-NT sensor with increasing HE4 concentration. The detection limit of the HE4/MIP-NT sensor is calculated as 0.2355 pM. On the other hand, the NIP-NT sensor shows a weaker response, with a slightly lower slope, indicating poor selectivity and sensitivity compared to the MIP sensor.

Figure 7 compares the responses of the multiplex FET biosensor across the two imprinted channels (CA125/MIP-NT and HE4/MIP-NT). It should be noted that the concentrations of CA125 and HE4 are presented in the conventional units commonly used for each biomarker in clinical practice and the relevant literature, namely U ml^{-1} and pM, respectively. Therefore, the comparison here is based on the relative signal response and selectivity of each imprinted channel toward its corresponding target analyte. On the CA125-imprinted channel, test solutions containing 0.1, 1, 10, and 100 U ml^{-1} CA125 produced signals that are 25.6-, 47.92-, 43.7-, and 34.6-fold higher, respectively, than those measured on the HE4-imprinted channel under identical conditions. The corresponding selectivity factor for the CA125/MIP-NT device is 11.3, indicating strong preference for CA125. On the HE4-imprinted channel, exposure to 0.01, 0.1, 1, and 5 pM HE4 gave signals 1.07-, 4.78-, 3.91-, and 2.91-fold higher than on the CA125-imprinted channel. This residual cross-response on the CA125-imprinted channel indicates

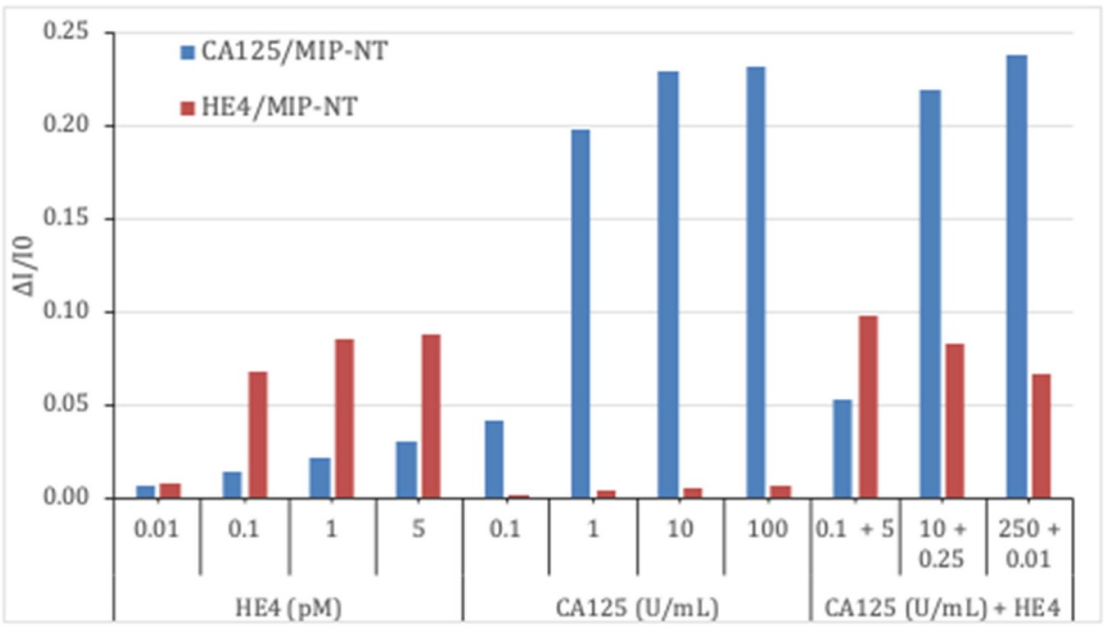

Figure 7. Responses of the multiplex CA125/MIP-NT and HE4/MIP-NT sensors to HE4 only, CA125 only and combination of both biomarkers.

partial recognition of smaller HE4 or nonspecific adsorption. On the other hand, the selectivity factor for the HE4/MIP-NT device is 23.7, demonstrating higher sensitivity and selectivity toward HE4.

When both proteins were introduced simultaneously, the CA125/MIP-NT channel showed no significant deviation from its signal response to CA125 alone. In contrast, the HE4/MIP-NT channel displayed a notable change: while the normalized current shift in response to 0.01 pM HE4 alone was only 0.75%, the signal increased to 6.7% when a mixture of 250 U ml^{-1} CA125 and 0.01 pM HE4 was applied.

These results indicate that the CA125/MIP-NT sensor exhibits high selectivity toward CA125 detection. Although the HE4/MIP-NT sensor demonstrates higher sensitivity to HE4, it also exhibits minor false-positive responses in the presence of CA125 in mixed samples. Despite this, the dual-channel FET sensor system offers an effective strategy for reducing error margins in multiplexed biomarker detection.

Tables 1 and table 2 summarize earlier reports on CA125 and HE4 detection, respectively, including the analytical methods, sensor platforms, linear dynamic ranges, and limits of detection. The wide differences in LOD and LDR among these studies indicate that sensor performance is strongly dependent on both the measurement approach and the platform design. For practical use in early detection, it is important to consider the typical concentration ranges of these biomarkers in blood. CA125 is commonly evaluated around a clinical threshold of 35 U ml^{-1}, but in early-stage disease its levels are often only slightly elevated and may remain within or just above this range [26]. Similarly, HE4 concentrations associated with early-stage diseases are typically found below 100 pM range [27]. Studies on prediagnostic samples have shown that both CA125 and HE4 can begin to increase up to 4 years before clinical diagnosis, highlighting the importance of detecting low biomarker concentrations [28]. In this context, the proposed sensor, with a linear detection range of 0.1–25 U ml^{-1} for CA125 and sub-picomolar sensitivity for HE4, is aligned with the concentration window relevant for early-stage detection. The MIP-based FET developed in this study, therefore, demonstrates competitive analytical performance and since it does not rely on antibodies, the proposed sensor also provides a practical alternative to conventional clinical detection methods.

Table 1. Comparison of existing studies on CA125 determination.

Sensing method	Linear detection range	Limit of detection	References
Label-free electrochemical immunosensor (antibody-modified electrode)	5–80 U ml^{-1}	1.45 U ml^{-1}	[29]
Electrochemical immunosensor (enzyme-assisted SWV, antibody-based)	0.0005–10 and 10–75 U ml^{-1}	6×10^{-6} U ml^{-1}	[30]
Optical aptasensor (UCNPs + aptamer, LRET mechanism)	0.01–100 U ml^{-1}	0.009 U ml^{-1}	[31]
Electrochemical immunosensor (BN nanosheets + antibodies)	5–100 U ml^{-1}	1.18 U ml^{-1}	[32]
Electrochemical immunosensor (MoS_2 + MOF nanocomposite)	0.0005–500 U ml^{-1}	0.0005 U ml^{-1}	[33]
SPR aptasensor (biotinylated DNA aptamer on Au surface)	10–100 U ml^{-1}	0.01 U ml^{-1}	[34]
FET biosensor (InSe 2D semiconductor channel + antibody functionalization)	0.01–1000 U ml^{-1}	0.01 U ml^{-1}	[35]
Electrochemical biosensor (MXene + PEI-crosslinked BSA antifouling layer)	0.01–1000 U ml^{-1}	0.0026 U ml^{-1}	[36]
FET biosensor (molecularly imprinted polypyrrole nanotubes via vapor deposition)	0.1–25 U ml^{-1}	0.4 U ml^{-1}	This work

Table 2. Comparison of existing studies on HE4 determination.

Sensing method & materials used	Linear detection range	Limit of detection	References
Label-free electrochemical immunosensor (3D PtNi nanocube-modified electrode + antibody)	0.001–100 ng ml^{-1}	0.00011 ng ml^{-1}	[37]
Electrochemiluminescence (ECL) immunosensor (Eu MOF@isoluminol + CdS quantum dots + Cu single-atom catalyst)	0.005–500 ng ml^{-1}	0.00158 ng ml^{-1}	[38]
Electrochemical immunosensor (MOF-based electrode + AuNPs + Prussian blue signal probe)	0.1–80 ng ml^{-1}	0.02 ng ml^{-1}	[39]
Optical immunosensor (self-assembled Au surface + protein G + antibody layer)	69.4–300.7 ng ml^{-1}	1.79 ng ml^{-1}	[40]
FET biosensor (molecularly imprinted polypyrrole (PPy) nanotubes via vapor deposition)	0.05–10 pM (0.001 25–0.25 ng ml^{-1})	0.2 pM (0.005 ng ml^{-1})	This work

4. Conclusion

In this study, we successfully fabricated a highly selective and sensitive multiplex FET biosensor for simultaneous detection of ovarian cancer biomarkers CA125 and HE4 using CA125- and HE4-imprinted PPy nanotubes. The template-assisted vapor deposition polymerization technique allowed for the formation of uniform PPy nanotubes with molecularly imprinted sites, which provided the sensor with the ability to selectively recognize and bind to CA125 or HE4. The MIP sensor produced a linear response, significantly outperforming the NIP sensor, which is limited by non-specific interactions. The sensor response was notably superior for CA125 or HE4 biomarkers, with a clear distinction between MIP and NIP sensors, confirming the effectiveness of molecular imprinting for specific biomarker detection. The developed MIP-based FET biosensor's ability to simultaneously detect multiple biomarkers highlights its potential for early and accurate cancer detection, offering a cost-effective alternative to antibody-based immunosensors.

Author contribution statement

FC: Conceptualization; Methodology; Investigation; Formal analysis; Data curation; Visualization; Writing—original draft. **UUT, EY, ASE, ST:** Investigation; Resources; Validation. **GOI**: Conceptualization; Supervision; Funding acquisition; Project administration; Writing—review & editing. All authors reviewed and approved the final version of the manuscript.

Acknowledgment

This work was supported by the Scientific and Technological Research Council of Turkey (TUBITAK), Grant No: 119Z342.

Data availability statement

Data sets generated during the current study are available from the corresponding author on reasonable request.

Conflict of interest

There are no conflicts to declare.

ORCID iDs

Faruk Can 0000-0002-9651-123X
Elaheh Yousefimiab 0009-0007-1582-5442
Ali Sarp Ebil 0009-0005-3481-3477
Gozde Ozaydin Ince 0000-0003-3255-4940

References

[1] Zhou Y, Tao L, Qiu J, Xu J, Yang X, Zhang Y, Tian X, Guan X, Cen X and Zhao Y 2024 *Signal Transduct. Target Ther.* **9** 132
[2] Sharma S, Raghav R, O'Kennedy R and Srivastava S 2016 *Enzyme Microb. Technol.* **89** 15–30
[3] Hayrapetyan H, Tran T, Tellez-Corrales E and Madiraju C 2023 *ELISA: Methods and Protocols* **1** 1–17
[4] Shevchenko K G, Garkushina I S, Canfarotta F, Piletsky S A and Barlev N A 2022 *RSC Adv.* **12** 3957–68
[5] El-Schich Z, Zhang Y, Feith M, Beyer S, Sternbæk L, Ohlsson L, Stollenwerk M and Wingren A G 2020 *Biotechniques* **69** 406–19
[6] Kang M S, Cho E, Choi H E, Amri C, Lee J H and Kim K S 2023 *Biomater. Res.* **27** 45
[7] Wang J, Chen D, Huang W, Yang N, Yuan Q and Yang Y 2023 *Exploration* **3** 20210027
[8] Madhivanan K, Atchudan R, Arya S and Sundramoorthy A K 2024 *Oral. Oncol. Rep.* **10** 100363
[9] Sakata T, Nishitani S and Kajisa T 2020 *RSC Adv.* **10** 16999–7013
[10] Zhou Q, Sasaki Y, Ohshiro K, Fan H, Montagna V, Gonzato C, Haupt K and Minami T 2022 *J. Mater. Chem. B* **10** 6808–15
[11] Rebelo P, Costa-Rama E, Seguro I, Pacheco J G, Nouws H P, Cordeiro M N D and Delerue-Matos C 2021 *Biosens. Bioelectron.* **172** 112719
[12] McClements J *et al* 2022 *ACS Sens.* **7** 1122–31
[13] Xu S, Wang L and Liu Z 2021 *Angew Chem., Int. Ed.* **60** 3858–69
[14] Akgönüllü S, Kılıç S, Esen C and Denizli A 2023 *Polymers* **15** 629
[15] Nishitani S, Sakata T and Kajisa T 2016 *Proc. IEEE Biomedical Circuits and Systems Conf.* 30–33
[16] Yang J C, Lim S J, Cho C H, Hazarika D, Park J P and Park J 2023 *Sens. Actuators B* **390** 133982
[17] Bartold K, Iskierko Z, Borowicz P, Noworyta K, Lin C Y, Kalecki J, Sharma P S, Lin H Y and Kutner W 2022 *Biosens. Bioelectron.* **208** 114203
[18] Mukherjee P, Dutta P, Sinha K, Sen S, Shirke T, Ganguly R, Barui A and RoyChaudhuri C 2023 *Appl. Phys. Lett.* **123** 193701
[19] Sasaki Y, Zhang Y, Fan H, Ohshiro K, Zhou Q, Tang W, Lyu X and Minami T 2023 *Sens. Actuators B* **382** 133458
[20] Kuntamung K, Jakmunee J and Ounnunkad K 2021 *J. Mater. Chem. B* **9** 6576–85
[21] Timilsina S S, Jolly P, Durr N, Yafia M and Ingber D E 2021 *Acc. Chem. Res.* **54** 3529–39
[22] O'Brien C, Khor C K, Ardalan S and Ignaszak A 2024 *Front. Med. Technol.* **6** 1360510
[23] Kwon O S, Park S J and Jang J 2010 *Biomaterials* **31** 4740–7
[24] Yoon H, Kim J H, Lee N, Kim B G and Jang J 2008 *Chem. Bio. Chem.* **9** 634–41
[25] Can F, Akkas T, Bekler S Y, Takmakli S, Uzun L and Ince G O 2024 *Bioelectrochem.* **157** 108655
[26] Charkhchi P, Cybulski C, Gronwald J, Wong F O, Narod S A and Akbari M R 2020 *Cancers* **12** 3730
[27] Dochez V, Caillon H, Vaucel E, Dimet J, Winer N and Ducarme G 2019 *J. Ovarian Res.* **12** 28
[28] Gislefoss R E, Langseth H, Bolstad N, Nustad K and Mørkrid L 2015 Int *J. Gynecol. Cancer* **25** 1608–15
[29] de Castro A C H, Alves L M, Siquieroli A C S, Madurro J M and Brito-Madurro A G 2020 *Microchem J.* **155** 104746
[30] Pakchin P S, Fathi M, Ghanbari H, Saber R and Omidi Y 2020 *Biosens. Bioelectron.* **153** 112029
[31] Zhang X, Wang Y, Deng H, Xiong X, Zhang H, Liang T and Li C 2021 *Microchem J.* **161** 105761
[32] Öndes B, Evli S, Uygun M and Uygun D A 2021 *Biosens. Bioelectron.* **191** 113454
[33] Li S, Hu C, Chen C, Zhang J, Bai Y, Tan C S, Ni G, He F, Li W and Ming D 2021 *ACS Appl. Bio Mater.* **4** 5494–502
[34] Shahbazlou S V, Vandghanooni S, Dabirmanesh B, Eskandsani M and Hasannia S 2023 *Microchem J.* **194** 109276
[35] Ji H, Wang Z, Wang S, Wang C, Zhang K, Zhang Y and Han L 2023 *Biosensors* **13** 193
[36] Li R, Yu K, Fan G-C, Song Z and Luo X 2024 *Sens. Actuators B* **408** 135520
[37] Chen D-N, Jiang L-Y, Zhang J-X, Tang C, Wang A-J and Feng J-J 2022 *Mikrochim. Acta.* **189** 455
[38] Tang Y, Liu Y, Xia Y, Zhao F and Zeng B 2023 *Anal. Chem.* **95** 4795–802
[39] Xu X, Tang L, Yu Y, Zhang J, Zhou X, Zhou T, Xuan C, Tian Q and Pan D 2024 *Biosens. Bioelectron.* **262** 116541
[40] Wang B, Liang G, Meng L, Li H, Song Z, Xu Y, He Y, Duan D, Shi Q and Gong Y 2025 *Sensors* **25** 3347